Nonadiabatic Electron Dynamics in Orthogonal Two-Color Laser Fields with Comparable Intensities

Ji-Wei Geng,[1] Wei-Hao Xiong,[1] Xiang-Ru Xiao,[1] Liang-You Peng,[1,2,*] and Qihuang Gong[1,2]
[1]*State Key Laboratory for Mesoscopic Physics and Department of Physics, Peking University, Beijing 100871, China*
[2]*Collaborative Innovation Center of Quantum Matter, Beijing 100871, China*

(Received 7 May 2015; published 4 November 2015)

We theoretically investigate the nonadiabatic subcycle electron dynamics in orthogonally polarized two-color laser fields with comparable intensities. The photoelectron dynamics is simulated by exact solution to the 3D time-dependent Schrödinger equation, and also by two other semiclassical methods, i.e., the quantum trajectory Monte Carlo simulation and the Coulomb-corrected strong field approximation. Through these methods, we identify the underlying mechanisms of the subcycle electron dynamics and find that both the nonadiabatic effects and the Coulomb potential play very important roles. The contribution of the nonadiabatic effects manifest in two aspects, i.e., the nonadiabatic ionization rate and the nonzero initial velocities at the tunneling exit. The Coulomb potential has a different impact on the electrons' trajectories for different relative phases between the two pulses.

DOI: 10.1103/PhysRevLett.115.193001 PACS numbers: 32.80.Rm, 33.20.Xx, 33.60.+q

Advances in attosecond technologies have opened up unprecedented opportunities for timing and controlling the electronic dynamics in atoms and molecules [1,2]. A crucial step for attosecond physics is to realize a stable and controllable electric field waveform of an optical pulse [3–5] so that the tunneling dynamics and the subsequent motion of the electron can be controlled [6–8]. The structural or dynamical information of the system can be retrieved by measuring the harmonic generation spectra or the differential distributions of the photoelectrons [9–13]. Among many other approaches to shape the optical wave form, the orthogonally polarized two-color (OTC) scheme has proved to be a simple but powerful tool to steer the motion of the electrons both temporally and spatially [14–24].

Depending on the value of the Keldysh parameter $\gamma = \omega\sqrt{2I_p}/E_0$ [25], the photoionization can be distinguished by the tunneling ($\gamma \ll 1$) and multiphoton ($\gamma \gg 1$) regimes. Here, ω and E_0 are the laser field frequency and amplitude, respectively, and I_p is the ionization potential. Despite the above applications of the OTC scheme in various subjects, it was only recently that there have been several experiments on a differential measurement of the photoelectrons in the context of OTC fields [26,27]. Similar to many other experiments performed with linearly or elliptically polarized laser fields, an adiabatic tunneling of the electron is treated as the starting point to interpret these data. In the adiabatic model, it is assumed that the electron tunnels through a static or quasistatic barrier formed by the electric field and the binding potential of the atom [28]. However, many strong-field experiments are performed in the intermediate range of $\gamma \sim 1$, where the concept of nonadiabtic tunneling should be adopted [29,30]. In the nonadiabatic picture, the electron tunnels through a time-dependent barrier, under which the electron acquires energy. In the case of the elliptically or circularly polarized field, the barrier is rotating in time and the electron cannot adiabatically follow the change of the barrier. For nonadiabatic effects in circularly polarized laser fields, the nonzero initial transverse momentum at the tunneling exit has recently attracted a lot of attention [31–38]. However, for circularly polarized laser fields, one cannot observe subcycle interference structures, which contain rich information of structures and dynamics. We show here by applying an OTC field, the subcycle interference can be effectively controlled and significant nonadiabatic effects can be identified.

The electric field of the OTC pulses can be expressed as $\mathbf{E}(t) = E_0[f_1(t)\cos(\omega_1 t)\hat{\mathbf{z}} + \beta f_2(t)\cos(\omega_2 t + \Delta\varphi)\hat{\mathbf{x}}]$, where β and $\Delta\varphi$, respectively, represent the ratio of the electric field strength and the relative phase of the two linearly polarized pulses. According to the value of β, the OTC schemes can be roughly divided into two different categories: when β is much smaller than 1, the second pulse only acts as a weak probe or control pulse and does not significantly contribute to the ionization [27]; on the contrary, when $\beta \sim 1$, the two pulses contribute to both ionization and propagation of the electronic wave packets (EWPs) [26]. For the case of the OTC field with comparable intensities, the initial tunneling ionization coordinates are determined by both pulses and the Keldysh parameter associated with the second harmonics is usually larger than one. In this situation significant nonadiabatic effects are expected to emerge.

In this Letter, we systematically investigate the nonadiabatic subcycle dynamics of EWPs generated from a H atom in the OTC field with comparable intensities by three different methods, i.e., the exact solution to the 3D time-dependent Schrödinger equation (TDSE) [39,40], the adiabatic quantum-trajectory Monte Carlo (QTMC) simulation [41,42], and the nonadiabatic Coulomb-corrected strong-field-approximation (CCSFA) [43–45]. Both the QTMC and CCSFA methods fully consider the effects of the Coulomb potential in the electron's trajectory propagation. The integration of the classical action for each trajectory in both methods allows one to trace the origins of the interferences in the resultant momentum distributions. Depending on $\Delta\varphi$, the electron trajectories are controlled by electric fields of both pulses and the ionic Coulomb potential, which lead to very complicated interference structures in the final momentum distributions. We successfully disentangle different contributions to the distinctive interference structures in each domain of the electron momentum distribution. Comparing the results of these two semiclassical methods with the TDSE calculations, we find clear evidence of the nonadiabatic effects, i.e., the nonadiabatic ionization rate and the nonzero initial velocities at the tunneling exit, which will dramatically influence the momentum spread and the interference visibility of the ionized EWPs. Moreover, we demonstrate that the Coulomb potential plays important roles in the EWP dynamics. We conclude that the electron's dynamics is jointly determined by the nonadiabatic effects at the tunneling exit and the role of the Coulomb potential in the electron's propagation process. We show that all these effects can be manipulated by changing $\Delta\varphi$ of the OTC pulse.

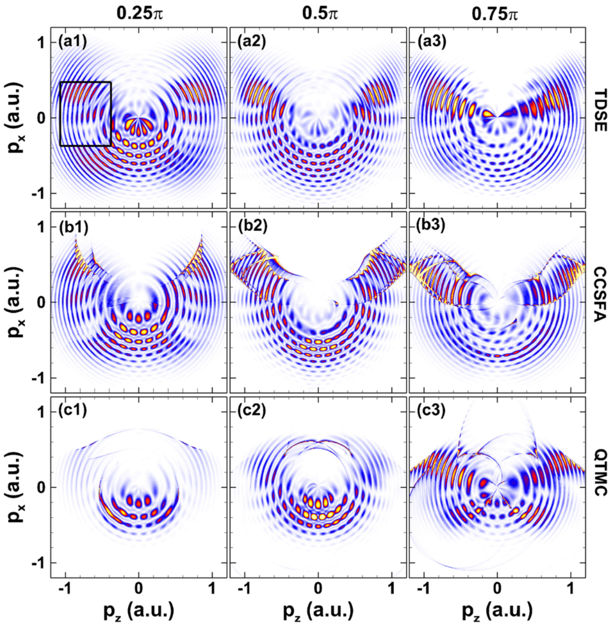

FIG. 1 (color online). Electron momentum distributions in the polarization plane of the OTC field with three different $\Delta\varphi$ (shown on top of each column), respectively, calculated by the TDSE (first row), CCSFA (second row), QTMC (third row) methods. The black rectangle in (a1) marks the interference patterns caused by the EWP $w1$ and $w2$ for $\Delta\varphi = 0.25\pi$; see Fig. 2(a) for an illustration.

In our calculations, the OTC field is synthesized by a four-cycle trapezoidal $(1+2+1)$ laser pulse at 800 nm in $\hat{\mathbf{z}}$ with its second harmonic (400 nm) in $\hat{\mathbf{x}}$. In the following, we only focus on discussion the case of $\beta = 1$ with an equal peak intensity of $I_0 = 1\times 10^{14}$ W/cm^2, since the resultant electron spectra are similar and our main conclusions hold when the intensity of the second harmonic is varied around I_0 within 25%. Figure 1 shows the electron momentum distributions calculated by the three different methods (in each row) in the polarization plane, for three different $\Delta\varphi$ (in each column). From the *ab initio* TDSE calculations [Figs. 1(a1)–1(a3)], we can see that the momentum distributions and the interference patterns are sensitively dependent on $\Delta\varphi$. For example, for the cases of 0.25π and 0.75π, both the recent experimental measurements [26] and our TDSE results show distinctive differences. The CCSFA method faithfully reproduces all the main features of the exact TDSE results except some inevitable caustics [44] in the $p_x > 0$ plane. However, the QTMC simulation only qualitatively gives part of the interference patterns with an underestimate of the global size of the momentum spread and inaccurate description of the relative yield in each domain of the momentum plane. First, we will show how the interferences among the EWPs are manipulated by changing $\Delta\varphi$.

Different from the streaking case [27], there are four significant EWPs (instead of two) generated in each fundamental laser cycle. The ionization rates and the emission times of the four EWPs can be controlled by changing the relative phase of the two pulses. To identify the subcycle interference patterns formed by changing $\Delta\varphi$, in Fig. 2(a), we schematically illustrate the electric field within one cycle of the 800 nm pulse for $\Delta\varphi = 0.25\pi$, together with the four peaks of the ionization rates. Also shown in Fig. 2(a) is the resultant momentum distribution simulated by the strong field approximation (SFA) *without* consideration of the interference among the four EPWs (denoted by $w1$–$w4$). However, the interferences among the EWPs will significantly alter the final momentum distributions in the polarization plane, as shown in Figs. 2(b)–2(e) for four different $\Delta\varphi$. Apparently, by varying $\Delta\varphi$, one can control the emission time, the ionization rate, and the phase accumulation of each EWP, which all change the interference fringes' space, shape, and contrast in the final momentum distributions. The gross interference patterns can be analyzed within the framework of SFA by the phase difference accumulated in the laser fields for two EWPs, i.e., $\Delta S = \int_{t_1}^{t_2} d\tau\{\frac{1}{2}[\mathbf{p}+\mathbf{A}(\tau)]^2 + I_p\}$, where t_1 and t_2 is the birth time of each EWP. The position of the interference maxima can then be expressed as a series of circles given by $(p_x + F_x/\Delta t)^2 + (p_z + F_z/\Delta t)^2 = R^2$, where $\Delta t = t_2 - t_1$, $\mathbf{F} = \int_{t_1}^{t_2} d\tau \mathbf{A}(\tau)$, and R is a constant related to the laser parameters and I_p. One notes that for $\Delta\varphi = 0.25\pi$ and

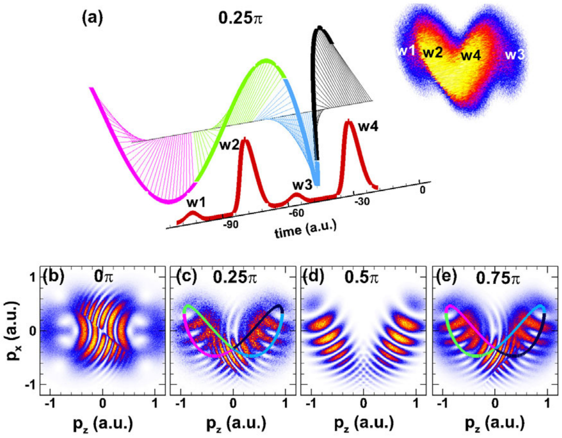

FIG. 2 (color online). (a) Illustration of the subcycle EWPs dynamics for $\Delta\varphi = 0.25\pi$. Four EWPs (denoted by $w1$–$w4$) are created at each cycle of the 800 nm pulse. (b)–(e) Subcycle interference patterns for different $\Delta\varphi$, calculated by SFA. Also shown upon the momentum distribution is $\mathbf{p} = -\mathbf{A}(t)$ for $\Delta\varphi = 0.25\pi$ and 0.75π, respectively, in (c) and (e) as color lines. Four different colors represent the timing sequence of the four EWPs as the same in (a).

0.75π, according to $\mathbf{p} = -\mathbf{A}(t)$, they should have the same momentum distribution. Indeed, one can see from Figs. 2(c) and 2(e) that the overlap of $w1$ and $w2$ for both cases forms very similar butterflylike interference patterns. However, the interference patterns close to $p_z = 0$ (caused by $w2$ and $w4$ for 0.25π, and by $w1'$ and $w3'$ for 0.75π) curve in different directions. This can be explained by observing the vector potential shown in Fig. 3(a). For the case of 0.25π, the integral of the vector potential along $\hat{\mathbf{x}}$ approximately equals to zero because $w2$ and $w4$ are separated by about one cycle of 400 nm, which is also the same for $w1'$ and $w3'$ in the case of 0.75π. On the contrary, the integral of the vector potential along $\hat{\mathbf{z}}$ is quite different for these two relative phases, i.e., $F_z < 0$ for 0.25π and $F_z > 0$ for 0.75π, which means that the interference rings will, respectively, center around ($p_x \simeq 0$, $p_z > 0$) for 0.25π and around ($p_x \simeq 0$, $p_z < 0$) for 0.75π. All the interference structures for different $\Delta\varphi$ can be qualitatively analyzed by the simple formula given above.

The above interference analysis based on SFA for a single-cycle case gives a global view of how the four EWPs are generated and the critical dependence of the momentum distributions on $\Delta\varphi$. For the case of multiple-cycle pulses with the consideration of the Coulomb potential, the gross interference features are still visible but with the superpositions of the intercycle interferences, as shown in Fig. 1. In addition, the relative yields in each domain in the momentum plane are drastically influenced by the Coulomb potential. Both the QTMC and the CCSFA methods qualitatively reproduce the main features of the TDSE results. However, the CCSFA has a much better performance than the QTMC method.

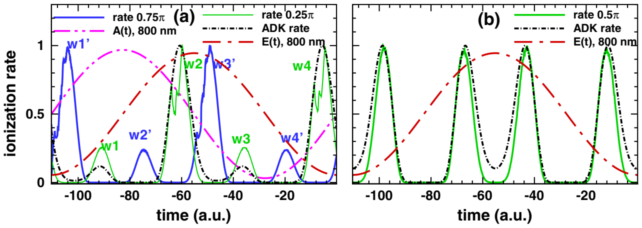

FIG. 3 (color online). (a) Ionization rates extracted from the CCSFA for $\Delta\varphi = 0.25\pi$ (solid thin green) and 0.75π (solid thick blue), respectively. Also shown are the ADK rate (black dashed-dotted) for the QTMC method at 0.25π and the laser fields for the 800 nm pulse. (b) Same as (a) but for $\Delta\varphi = 0.5\pi$.

We now turn to discuss to the nonadiabatic effects in the OTC context, manifested in both the ionization rate and the nonzero initial velocities at the tunneling exit. As shown in Fig. 1, the QTMC method only qualitatively reproduces part of the main features in the TDSE results. For example, the butterflylike interference patterns marked by the black rectangle in Fig. 1(a1) are almost absent in Fig. 1(c1) by the QTMC calculations, which are, however, well reproduced by the CCSFA method. We will show that these discrepancies originate from the nonadiabatic effects. The ionization rate is given adiabatically in the QTMC method by the ADK formula and nonadiabatically implied in the CCSFA method. In Fig. 3(a), we show the normalized ionization rates from both methods. For the case of 0.25π, one finds that the ionization rate of the EWPs $w1$ and $w3$ calculated by the CCSFA method is significantly higher than the ADK rate [28] for the QTMC method. As mentioned above, the interference patterns in the black rectangle come from the overlap of the EWPs $w1$ and $w2$. A lower ionization rate of the wave packet $w1$ leads to a low interference contrast. On the contrary, for $\Delta\varphi = 0.5\pi$ [Fig. 3(b)], the normalized ionization rate of each EWP is almost the same for the QTMC and the CCSFA method. Therefore, at 0.5π we can turn to investigate another type of nonadiabatic effect, i.e., the nonzero initial velocities at the tunneling exit [33–35,42]. The Coulomb potential is incorporated only in the propagation process in our QTMC and CCSFA calculation and thus does not influence the initial momentum distribution. So we can choose to "turn off" the Coulomb potential in the semiclassical model, and for a better comparison we only incoherently sum the electron's final momentum in the same bin to exclude the interference effects. Figure 4(a) shows the final momentum distribution for $\Delta\varphi = 0.5\pi$ calculated by CCSFA with $p_z < 0$ and QTMC with $p_z > 0$, respectively. A distinct difference in the momentum spread can be found between these two models. The moment t_1 in Fig. 4(a) illustrates the negative value of the vector potential when the ionization rate reaches its maxima. We can see that the most probable electrons calculated by the QTMC are well located on the line predicted by the classical description $\mathbf{p} = -\mathbf{A}(t_1)$, while the most probable electrons calculated by the CCSFA

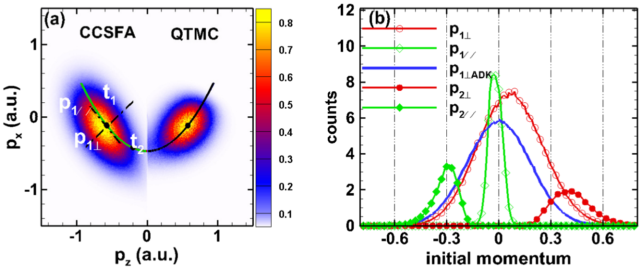

FIG. 4 (color online). (a) Momentum distribution for $\Delta\varphi = 0.5\pi$, respectively, calculated by the CCSFA and the QTMC methods. The green and black solid curves shows $\mathbf{p} = -\mathbf{A}(t)$. (b) The initial transverse and longitudinal momentum distributions extracted from the CCSFA, respectively, at time t_1 and t_2, marked in (a). The full blue line represents the initial transverse momentum distribution obtained by the QTMC model.

are notably larger than this prediction. Actually, in the CCSFA method the final momentum is given by $\mathbf{p} = \mathbf{p}_{\text{ini}} - \mathbf{A}(t)$. In the following, we will show that this nonzero initial momentum $\mathbf{p}_{\text{ini}}$ at the tunneling exit contributes to these discrepancies between the CCSFA and the QTMC methods.

In both of the two semiclassical methods, the initial momentum distributions at the tunneling exit can be easily extracted. Figure 4(b) shows the extracted initial longitudinal and transverse momentum for both methods at time t_1 and t_2, respectively. For the QTMC method, the initial momentum is known to be a Gaussian-like distribution for the transverse momentum $p_{1\perp\text{ADK}}$ [the blue line in Fig. 4(b)], and the longitudinal momentum is set to be zero. Also shown in Fig. 4(b) are the initial transverse (circles) and longitudinal (diamonds) momentum distribution extracted from the CCSFA method, for time t_1 (open symbols) and t_2 (filled symbols), respectively. At time t_1, both the transverse and longitudinal momentum have a Gaussian-like distribution, whose peaks are centered at a *nonzero* value, with the latter one having a much narrower width. For the time t_2 at which the ionization rate is much lower, both the initial transverse and longitudinal momentum distributions are centered at a much bigger nonzero value. Meanwhile, one sees that the width of the initial longitudinal momentum distribution for t_2 is larger than that of t_1. The nonzero central value of the initial transverse momentum leads to the deviation of the final momentum from the classical prediction $\mathbf{p} = -\mathbf{A}(t)$. The increasing width of the nonzero initial longitudinal momentum distribution as the decrease of the ionization rate leads to a larger momentum spread along the direction of $\mathbf{p} = -\mathbf{A}(t)$. Furthermore, we have calculated the central value of the initial momentum for different $\Delta\varphi$ at the moment when the electric field of the OTC pulse reaches its maximum. We find that both the nonzero initial transverse and longitudinal momentum are the largest at $\Delta\varphi = 0.5\pi$.

Both the nonadiabatic ionization rate and the nonzero initial velocities at the tunneling exit determine the initial coordinates of the tunneling electrons in the semiclassical model. We now give a more detailed discussion on the impact by the Coulomb potential. The Coulomb potential significantly influences the electron trajectories in the propagation process for different relative phases of the two pulses. Without the Coulomb potential, the gross structures of the momentum distribution are similar for $\Delta\varphi = 0.25\pi$ and 0.75π. In the accurate TDSE calculations [Figs. 1(a1) and 1(a3)], most of the electrons for $\Delta\varphi = 0.25\pi$ are driven to the $p_x < 0$ plane, while most of the electrons form narrower stripe structures in the $p_x > 0$ plane for $\Delta\varphi = 0.75\pi$. These differences in the subcycle dynamics can be analyzed by the CCSFA method for the dominant EWP $w1'$ for 0.75π and EWP $w2$ for 0.25π, respectively [cf., Fig. 3(a)]. The tunneling exit of these two EWPs are determined by $\mathbf{r}_0(t) = \int_{t_s}^{t} dt'[\mathbf{p}_0 + \mathbf{A}(t')]$, where $\mathbf{p}_0$ is the asymptotic momentum without the Coulomb correction and t_s satisfies the saddle point equation $[\mathbf{p}_0 + \mathbf{A}(t_s)]^2 = -2I_p$. We note that the different emission time of these two EWPs [Fig. 3(a)] will lead to a different tunneling exit, i.e., for $w2$: $z < 0$ and $x > 0$, for $w1'$: $z > 0$ and $x < 0$. With the consideration of the Coulomb potential, the electron's final asymptotic momentum can be expressed as $\mathbf{p} = \mathbf{p}_0 - \int_{\text{Re}(t_s)}^{\infty}[\mathbf{r}(t)/r^3(t)]dt$. Neglecting the Coulomb potential, the asymptotic momentum $\mathbf{p}_0$ is the same for these two EWPs. Then the Coulomb correction to the undisturbed momentum $\mathbf{p}_0$ is given by $\Delta\mathbf{p} = -\int_{\text{Re}(t_s)}^{\text{Re}(t_s)+\Delta t}[\mathbf{r}(t)/r^3(t)]dt - \int_{\text{Re}(t_s)+\Delta t}^{\infty}[\mathbf{r}(t)/r^3(t)]dt \approx -[\mathbf{r}(t_r)/r^3(t_r)]\Delta t$, where Δt is a small time interval and t_r is the real part of t_s. In this time interval the electron is around the core and the Coulomb force is most important; after a time of Δt the electron will travel away and the Coulomb potential can be ignored. We can see that $\Delta\mathbf{p}$ is strongly affected by the tunneling exit. For $\Delta\varphi = 0.25\pi$: $z < 0$ and $x > 0$, the corresponding momentum distribution is shifted by the Coulomb field to the $\Delta p_z > 0$ and $\Delta p_x < 0$ domain, which leads to a higher ionization probability in the $p_x < 0$ plane. Similarly, the momentum distribution is shifted to the $\Delta p_z < 0$ and $\Delta p_x > 0$ domain for $\Delta\varphi = 0.75\pi$. The above analysis shows that, for an OTC field with a different $\Delta\varphi$, the tunneling exit is different, which will lead to a different influence of the Coulomb force when the electron is around the core immediately after the ionization.

In conclusion, we have carried out a systematical study over the complicated interference structures in the OTC context with comparable intensities. We successfully identified the physical mechanisms for the critical phase dependence of the subcycle electron dynamics. By comparing three different methods, i.e., the *ab initio* TDSE calculation, the adiabatic QTMC method, and the nonadiabatic CCSFA simulation, we identify the nonadiabatic effects in the OTC scheme. Our study provides a complete understanding of the important roles played by the Coulomb potential and by the nonadiabatic effects in the

OTC scheme. We believe the important effects identified in the present work can be experimentally observed in the near future with a high-resolution measurement.

This work is supported by National Natural Science Foundation of China (NNSFC) under Grant No. 11322437, by the National Program on Key Basic Research Project (973 Program) under Grant No. 2013CB922402, by NNSFC under Grants No. 11174016 and No. 11121091, and by the Program for New Century Excellent Talents in University (NCET).

---

[*] liangyou.peng@pku.edu.cn
http://www.phy.pku.edu.cn/~lypeng/

[1] F. Krausz and M. Ivanov, Rev. Mod. Phys. **81**, 163 (2009).
[2] L.-Y. Peng, W.-C. Jiang, J.-W. Geng, W.-H. Xiong, and Q. Gong, Phys. Rep. **575**, 1 (2015).
[3] T. Brabec and F. Krausz, Rev. Mod. Phys. **72**, 545 (2000).
[4] L. E. Chipperfield, J. S. Robinson, J. W. G. Tisch, and J. P. Marangos, Phys. Rev. Lett. **102**, 063003 (2009).
[5] A. Wirth *et al.*, Science **334**, 195 (2011).
[6] P. Eckle, M. Smolarski, P. Schlup, J. Biegert, A. Staudte, M. Schöffler, H. G. Muller, R. Dörner, and U. Keller, Nat. Phys. **4**, 565 (2008).
[7] P. Eckle, A. N. Pfeiffer, C. Cirelli, A. Staudte, R. Dörner, H. G. Muller, M. Büttiker, and U. Keller, Science **322**, 1525 (2008).
[8] D. Shafir, H. Soifer, B. D. Bruner, M. Dagan, Y. Mairesse, S. Patchkovskii, M. Y. Ivanov, O. Smirnova, and N. Dudovich, Nature (London) **485**, 343 (2012).
[9] D. Shafir, Y. Mairesse, D. M. Villeneuve, P. B. Corkum, and N. Dudovich, Nat. Phys. **5**, 412 (2009).
[10] J. Zhao and M. Lein, Phys. Rev. Lett. **111**, 043901 (2013).
[11] P. M. Kraus, D. Baykusheva, and H. J. Wörner, Phys. Rev. Lett. **113**, 023001 (2014).
[12] Y. Huismans *et al.*, Science **331**, 61 (2011).
[13] X. Xie, S. Roither, D. Kartashov, E. Persson, D. G. Arbó, L. Zhang, S. Gräfe, M. S. Schöffler, J. Burgdörfer, A. Baltuška, and M. Kitzler, Phys. Rev. Lett. **108**, 193004 (2012).
[14] Ph. Antoine, B. Piraux, and D. B. Milošević, and M. Gajda, Phys. Rev. A **54**, R1761 (1996).
[15] M. Kitzler and M. Lezius, Phys. Rev. Lett. **95**, 253001 (2005).
[16] I. J. Kim, C. M. Kim, H. T. Kim, G. H. Lee, Y. S. Lee, J. Y. Park, D. J. Cho, and C. H. Nam, Phys. Rev. Lett. **94**, 243901 (2005).
[17] M. Kitzler, X. Xie, A. Scrinzi, and A. Baltuska, Phys. Rev. A **76**, 011801 (2007).
[18] M. Kitzler, X. Xie, S. Roither, A. Scrinzi, and A. Baltuska, New J. Phys. **10**, 025029 (2008).
[19] H. Niikura, H. J. Wörner, D. M. Villeneuve, and P. B. Corkum, Phys. Rev. Lett. **107**, 093004 (2011).
[20] G. Laurent, W. Cao, H. Li, Z. Wang, I. Ben-Itzhak, and C. L. Cocke, Phys. Rev. Lett. **109**, 083001 (2012).
[21] L. Zhang, X. Xie, S. Roither, Y. Zhou, P. Lu, D. Kartashov, M. Schöffler, D. Shafir, P. B. Corkum, A. Baltuška, A. Staudte, and M. Kitzler, Phys. Rev. Lett. **112**, 193002 (2014).
[22] H. Yun, K. M. Lee, J. H. Sung, K. T. Kim, H. T. Kim, and C. H. Nam, Phys. Rev. Lett. **114**, 153901 (2015).
[23] X. Xie, Phys. Rev. Lett. **114**, 173003 (2015).
[24] X. Gong, P. He, Q. Song, Q. Ji, H. Pan, J. Ding, F. He, H. Zeng, and J. Wu, Phys. Rev. Lett. **113**, 203001 (2014).
[25] L. V. Keldysh, Sov. Phys. JETP **20**, 1307 (1965).
[26] L. Zhang, X. Xie, S. Roither, D. Kartashov, Y. L. Wang, C. L. Wang, M. Schöffler, D. Shafir, P. B. Corkum, A. Baltuška, I. Ivanov, A. Kheifets, X. J. Liu, A. Staudte, and M. Kitzler, Phys. Rev. A **90**, 061401(R) (2014).
[27] M. Richter, M. Kunitski, M Schöffler, T. Jahnke, L. P. H. Schmidt, M. Li, Y. Liu, and R. Dörner, Phys. Rev. Lett. **114**, 143001 (2015).
[28] M. V. Ammosov, N. B. Delone, and V. P. Krainov, Sov. Phys. JETP **64**, 1191 (1986).
[29] G. L. Yudin and M. Y. Ivanov, Phys. Rev. A **64**, 013409 (2001).
[30] M. Y. Ivanov, M. Spanner, and O. Smirnova, J. Mod. Opt. **52**, 165 (2005).
[31] I. Barth and O. Smirnova, Phys. Rev. A **84**, 063415 (2011).
[32] I. Barth and O. Smirnova, Phys. Rev. A **87**, 013433 (2013).
[33] T. Herath, L. Yan, S. K. Lee, and W. Li, Phys. Rev. Lett. **109**, 043004 (2012).
[34] J. Kaushal and O. Smirnova, Phys. Rev. A **88**, 013421 (2013).
[35] R. Boge, C. Cirelli, A. S. Landsman, S. Heuser, A. Ludwig, J. Maurer, M. Weger, L. Gallmann, and U. Keller, Phys. Rev. Lett. **111**, 103003 (2013).
[36] I. A. Ivanov and A. S. Kheifets, Phys. Rev. A **89**, 021402(R) (2014).
[37] M. Klaiber, K. Z. Hatsagortsyan, and C. H. Keitel, Phys. Rev. Lett. **114**, 083001 (2015).
[38] L. Torlina, F. Morales, J. Kaushal, I. Ivanov, A. Kheifets, A. Zielinski, A. Scrinzi, H. G. Muller, S. Sukiasyan, M. Ivanov, and O. Smirnova, Nat. Phys. **11**, 503 (2015).
[39] M. H. Xu, L.-Y. Peng, Z. Zhang, Q. Gong, X. M. Tong, E. A. Pronin, and A. F. Starace, Phys. Rev. Lett. **107**, 183001 (2011).
[40] M. V. Frolov, D. V. Knyazeva, N. L. Manakov, A. M. Popov, O. V. Tikhonova, E. A. Volkova, M.-H. Xu, L.-Y. Peng, L.-W. Pi, and A. F. Starace, Phys. Rev. Lett. **108**, 213002 (2012).
[41] M. Li, J.-W. Geng, H. Liu, Y. Deng, C. Wu, L.-Y. Peng, Q. Gong, and Y. Liu, Phys. Rev. Lett. **112**, 113002 (2014).
[42] J.-W. Geng, L. Qin, M. Li, W.-H. Xiong, Y. Liu, Q. Gong, and L.-Y. Peng, J. Phys. B **47**, 204027 (2014).
[43] S. Popruzhenko and D. Bauer, J. Mod. Opt. **55**, 2573 (2008).
[44] T. M. Yan, S. V. Popruzhenko, M. J. J. Vrakking, and D. Bauer, Phys. Rev. Lett. **105**, 253002 (2010).
[45] T. M. Yan and D. Bauer, Phys. Rev. A **86**, 053403 (2012).